nature communications

Article

https://doi.org/10.1038/s41467-025-64533-5

Metallocene-anchor inducing oriented MOF membrane for helium separation

Received: 7 May 2025

Accepted: 16 September 2025

Published online: 27 October 2025

Check for updates

Ju Bai[1,2,3], Luqi Xiao[1], Xiangping Zhang[1,3,4], Hongyan Liu[1,2,3], Can Wang[1], Lili Gong[1], Shuangjiang Luo[1,3], Yihan Zhu[5], Linglong Shan[1,3] ✉, Hongwei Fan[6] ✉ & Suojiang Zhang[1,7] ✉

Oriented metal-organic framework (MOF) membranes hold significant promise for advanced helium (He) separation, but their synthesis remains a challenging task. We report the preparation of an oriented MOF membrane using metal-organic polyhedra (MOP) fragment as metallocene-anchor. The metallocene-anchor induces the growth of homoligand Zr-MOF along the c-axis, resulting in the {001}-oriented structure. This orientation increases the transition energy barrier of methane (CH_4), enabling precise He/CH_4 separation with a selectivity of 77.3 and a He permeance of 695.1 GPU. The membrane exhibits exceptional robustness, demonstrating resistance to high-pressure conditions (up to 40 bar), thermal shock (−25 °C to 85 °C), and long-term stability (1000 h). The separation performance surpasses that of existing MOF membranes and exceeds the Robeson upper bound. Additionally, a three-stage membrane process enables the concentration of low He concentrations of 0.3% up to 99.9%, highlighting the potential of membranes for helium extraction. The successful fabrication of various oriented MOF membranes indicates the universality of this strategy.

Helium (He) is an irreplaceable commodity due to its distinct properties, making it essential for a variety of applications, including aerospace, industrial leak detection, nuclear magnetic resonance imaging, and welding[1]. It is primarily extracted on a large scale from natural gas through cryogenic distillation combined with pressure swing adsorption. However, high energy consumption and costs represent significant challenges associated with this technology. Membrane-based gas separation offers a promising alternative, providing a non-pollution, energy-efficient, and simpler way compared to traditional separation process[2]. The inaugural commercial membrane-based He extraction unit, installed in the 1980s, consumed only approximately 40% of the energy required by the cryogenic process[3]. While polymer membranes offer advantages in terms of processability and economic feasibility, they still undergo a trade-off between selectivity and permeance, as described by the Robeson upper bound. Therefore, achieving high performance in both areas while maintaining stable operation under harsh conditions remains a persistent challenge. There is an immediate need to design robust membranes for efficient industrial-scale applications.

Metal-organic frameworks (MOFs), composed of metal nodes and organic linkers, provide a strongly adjustable platform for structural design, enabling precise regulation of the pore-aperture size and/or shape at the gas molecule scale. This tunability has made MOFs a subject of extensive research for constructing molecular sieve

[1]Beijing Key Laboratory of Solid State Battery and Energy Storage Process, State Key Laboratory of Mesoscience and Engineering, Institute of Process Engineering, Chinese Academy of Sciences, Beijing, PR China. [2]Chengdu Institute of Organic Chemistry, Chinese Academy of Sciences, Chengdu, PR China. [3]University of Chinese Academy of Sciences, Beijing, PR China. [4]State Key Laboratory of Heavy Oil Processing, College of Chemical Engineering and Environment, China University of Petroleum, Beijing, PR China. [5]Center for Electron Microscopy, State Key Laboratory Breeding Base of Green Chemistry Synthesis Technology and College of Chemical Engineering, Zhejiang University of Technology, Hangzhou, PR China. [6]The State Key Laboratory of Chemical Resource Engineering, College of Chemical Engineering, Beijing University of Chemical Technology, Beijing, PR China. [7]Henan University, Zhengzhou, PR China. ✉e-mail: llshan@ipe.ac.cn; fanhongwei@mail.buct.edu.cn; sjzhang@ipe.ac.cn

membranes for gas separations[4–7]. MOFs typically feature multiple channels with specific pore-aperture in different crystallographic orientations. It has been confirmed that the oriented MOF membranes, with rigid aperture size and short diffusion path, are ideal for the membrane achieving the high selectivity and permeance simultaneously. Nevertheless, the preparation of oriented MOF membranes faces considerable challenges, particularly in designing the desired specific orientation for different gases. Common methods employed for oriented growth include the seeding and secondary growth[8–11], evolutionary growth[12–14], layer-by-layer growth[15–17], and in situ deposition (also called direct growth) on modified substrates[18,19]. Among the various MOFs, Zr-MOF is particularly noted for its superior chemical, thermal, and mechanical stability, ascribing to its high connectivity structure formed by high-valency metal ion (such as Zr^{4+}) coordinated to 8–12 ligands. While oriented Zr-MOF membranes are typically grown in the (111) direction[10,20–23], the {001}-oriented Zr-MOF membrane, which grows along the c-axis, has rarely been explored. The {001}-oriented Zr-MOF membrane, with its lower atomic packing density and smaller pore-aperture size, holds significant promise for the precise separation of He depending on a rigid molecular sieving.

Metal-organic polyhedra (MOP) have garnered significant interest due to their structural similarity to MOFs. Both are composed of metal ions and organic ligands via self-assembly, except that MOP have capping terminal groups that prevent indefinite expansion into networks[24,25]. It can be imagined that, based on the similarity of the self-assembly mechanism, the MOP can be employed to precisely regulate the oriented growth of MOFs. As a proof of concept, a metallocene-anchor induced strategy has been proposed to regulate the nucleation and growth of MOF along <001> orientation on the substrate, with the assistance of an electric field (Fig. 1a, b).

Results

Metallocene-anchored strategy induced the {001}-oriented growth of Zr-MOF

The Zr-MOF, Zr-MOP, and {001}-oriented Zr-MOF membranes were prepared by an electrochemical synthesis method under mild conditions, significantly reducing reaction time compared to conventional

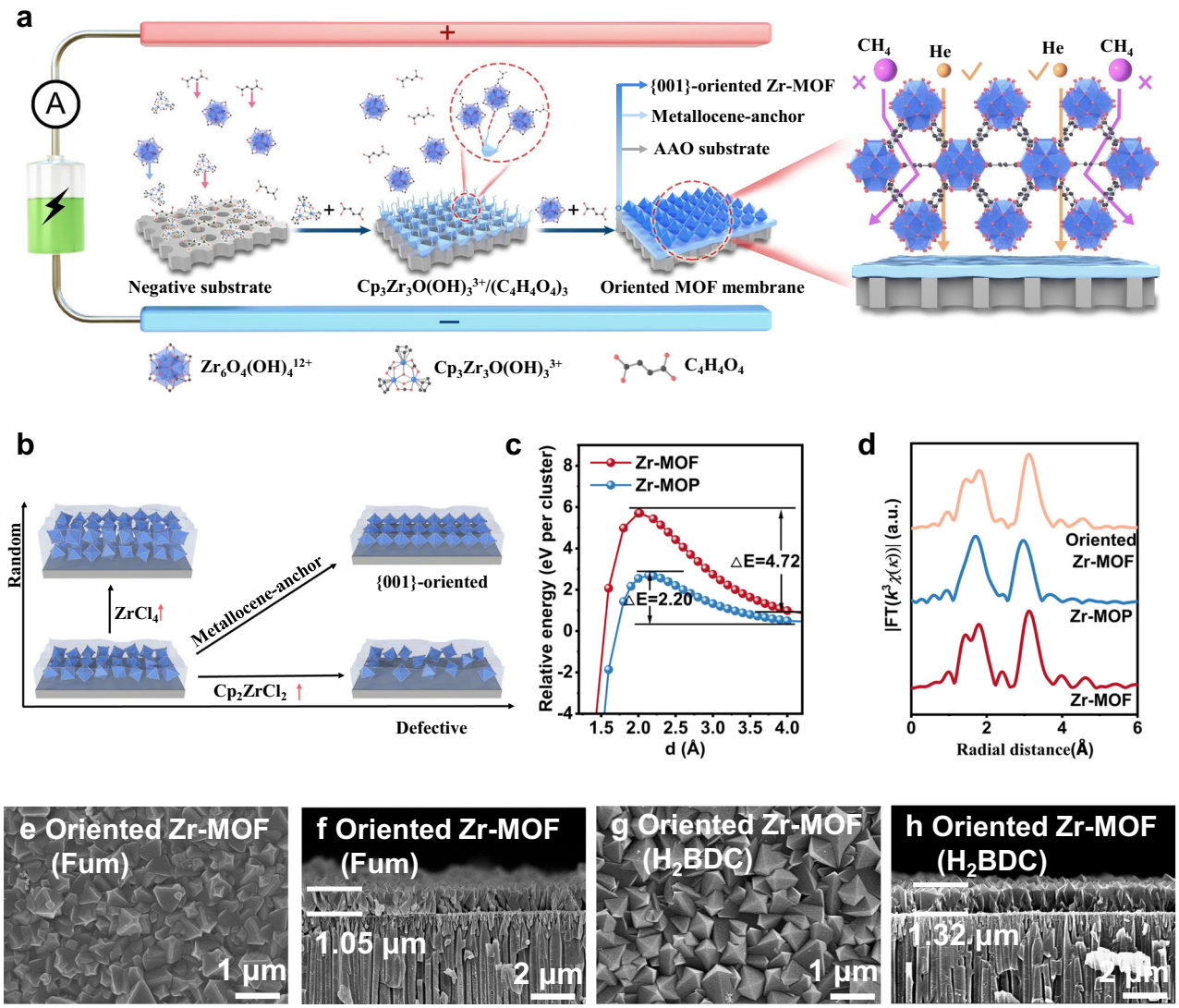

Fig. 1 | Metallocene-anchored strategy induced the orientation of the MOF membrane. a Oriented growth procedure and gases transportation behavior of the {001}-oriented Zr-MOF membrane. The Zr, O, and C atoms are represented by blue, red, and black, respectively. **b** Schematic illustration of the structural regulation of the {001}-oriented MOF membrane. **c** Potential energy barriers (ΔE) for the synthesis of Zr-MOF and Zr-MOP fragment. **d** EXAFS spectra for Zr-MOF, Zr-MOP, and {001}-oriented Zr-MOF. Surface and cross-sectional morphologies of (**e**, **f**) the {001}-oriented fumarate-based Zr-MOF and (**g**, **h**) the {001}-oriented H_2BDC-based Zr-MOF. Zr-MOF in the following sections represents fumarate-based Zr-MOF, where not specifically stated.

methods[5,26,27]. A conductive anodic aluminum oxide (AAO) disk as a substrate was vertically immersed in a precursor solution, which acted as a cathode under an electric field to facilitate the deprotonation of the ligand (fumarate) to promote the rapid growth of the MOF membrane (Supplementary Fig. 1). As expected, a continuous Zr-MOF membrane, built by the fumarate ligand and $ZrCl_4$ metal source grew on the substrate (Supplementary Fig. 2), with optimized preparation conditions (Supplementary Figs. 3–5). The Zr-MOP and Zr-MOF were synthesized, sharing the same ligand of fumarate but differing in metal source. Cp_2ZrCl_2, the metal source of Zr-MOP, was introduced into the precursor solution of Zr-MOF (including $ZrCl_4$ and fumarate) to induce the regular growth of the {001}-oriented Zr-MOF membrane on the substrate. To investigate the growth mechanism of the {001}-oriented Zr-MOF membrane, density functional theory (DFT) was employed to reveal the coordination process of the ligand and metal cluster (Fig. 1c), which involves a fumarate approaching an unsaturated coordination structure in a specific direction (Supplementary Fig. 6). The fragment unit consists of a typical Zr-cluster ($Zr_6O_4(OH)_4^{12+}$) connected with four fumarates for Zr-MOF, and a Zr-cluster ($Cp_3Zr_3O(OH)_3^{3+}$) connected with two fumarates for Zr-MOP, respectively. The energy scan shows that the fumarate needs to overcome a potential energy barrier of 2.20 eV to form Zr-MOP, less than that of 4.72 eV for Zr-MOF, which indicates Zr-MOP is preferentially generated over Zr-MOF in the precursor solution. This finding is further corroborated by the gradual color change of the reaction solution with time (Supplementary Figs. 7–9). Upon the addition of Cp_2ZrCl_2 to the precursor solution, no color change was observed. However, after 10 min of reductive electrochemical synthesis, the color of the precursor solution for the {001}-oriented Zr-MOF differed from that of pure Zr-MOF and resembled that of Zr-MOP. With a reaction time increased to 20 min, the color of the precursor solution for the {001}-oriented Zr-MOF approximated that of pure Zr-MOF. This color transition demonstrates that the coordination of Cp_2ZrCl_2 occurs prior to $ZrCl_4$, consistent with the results of the DFT, thereby regulating the growth of Zr-MOF to a certain extent. Under the influence of the applied electric field, $Cp_3Zr_3O(OH)_3^{3+}$ and $Zr_6O_4(OH)_4^{12+}$ are drawn toward the negatively charged AAO substrate, and $Cp_3Zr_3O(OH)_3^{3+}$ reacts with fumarate preferentially. Then the positively charged Zr-cluster combined with AAO and the three negatively charged fumarate (deprotonation) stands upright due to the electrostatic repulsion. Furthermore, the fumarate and $Zr_6O_4(OH)_4^{12+}$ alternately coordinate along the anchored $Cp_3Zr_3O(OH)_3^{3+}$/fumarate (metallocene-anchored), resulting in the vertical growth of the Zr-MOF (Fig. 1a and Supplementary Fig. 10). The significant morphological changes in the membrane reflect the probable vertical orientation of the Zr-MOF membrane (Fig. 1e, g), with a thickness of approximately 1 μm (Fig. 1f, h) and a higher roughness of 74.8 nm (Supplementary Fig. 11).

Furthermore, the trace of Cp_2ZrCl_2 was tracked to confirm the successful transition of the metallocene-anchor induced {001}-oriented Zr-MOF structure. The attenuated total reflectance Fourier transform infrared (ATR-FTIR) spectra of the {001}-oriented Zr-MOF membrane and the Zr-MOF membrane were nearly identical (Supplementary Fig. 12). However, it can be seen in the enlarged area that the cyclopentadienyl signal of Cp_2ZrCl_2 appears at around 1022 cm^{-1} and 802 cm^{-1} for the {001}-oriented Zr-MOF membrane[28], providing clear evidence of the formation of the metallocene-anchor in the {001}-oriented Zr-MOF membrane. Additionally, X-ray photoelectron spectroscopy (XPS) analysis revealed that the {001}-oriented Zr-MOF membrane exhibited a higher binding energy for Zr 3*d* than Zr-MOF membrane, suggesting fewer open metal sites for the {001}-oriented Zr-MOF membrane surface (Supplementary Fig. 13)[29], which means the {001}-oriented Zr-MOF membrane structure possesses a higher coordination saturation and fewer molecular level defects. The specific surface area of the Zr-MOP, Zr-MOF, and {001}-oriented Zr-MOF was assessed using N_2 adsorption (Supplementary Fig. 14), revealing that the {001}-oriented Zr-MOF exhibited the highest specific surface area of 469.8 $m^2 g^{-1}$. Furthermore, in comparison to the Zr-MOF that has two prominent pore size distribution peaks at 0.98 nm and 1.17 nm, the pore size of the {001}-oriented Zr-MOF decreased to 0.86 nm and 1.17 nm, respectively. We observed a decrease in one of the peaks from 0.98 nm to 0.86 nm, ascribing to the introduction of the larger cyclopentadienyl group. To validate the metallocene-anchored strategy, fumarate was substituted with terephthalic acid (H_2BDC), and the obviously the {001}-oriented UiO-66 formed as expected (Fig. 1g, h and Supplementary Fig. 15). In addition, we successfully prepared vertical MOF membranes on series substrate of carbon paper and aluminum oxide substrates for various applications (Supplementary Figs. 16–18). These findings demonstrate the universality of this metallocene-anchor induced {001}-oriented growth strategy.

The local coordination environment around Zr ions was investigated using X-ray absorption fine structure to quantitatively understand the component proportion of Zr-MOF and Zr-MOP[30]. X-ray absorption near-edge structure analysis revealed the sample valence order is approximately ZrO_2 > Zr-MOF ≈ {001}-oriented Zr-MOF > Zr-MOP > Zr foil (Supplementary Fig. 19). Extended X-ray absorption fine structure (EXAFS) spectra provided insights into the changes in the coordination number around Zr, and fitting analysis of Zr-MOF, Zr-MOP, and {001}-oriented Zr-MOF (Fig. 1d and Supplementary Figs. 20–22 and Supplementary Table 1). Firstly, the nearest neighbor of the Zr ion is the Zr-O shell, corresponding to the Zr-O$\mu_{3\text{-}O}$ and Zr-O_{COO} bonds at 1.8 Å and 2.3 Å, respectively[31]. The second peak corresponds to the Zr···Zr shell at 3.5 Å[32]. For strict consideration, the first shell of Zr-MOP is written in the form of Zr-C/O, indicating that this site may be C or O. Zr-MOP exhibits a larger bond length Zr-C signal at 2.6 Å compared to Zr-MOF. Under rigorous consideration, the first shell of Zr-MOP was written in the form of Zr-C/O, indicating that this site may be C or O. It can be seen from the EXAFS diagram that {001}-oriented Zr-MOF contains both Zr-MOF and Zr-MOP coordination environments. In contrast, the structure of {001}-oriented Zr-MOF is more similar to Zr-MOF than Zr-MOP, which indicates that the Zr-MOP fragment only plays an induction role and the dominant structure of the membrane remains Zr-MOF.

Orientation analysis of the Zr-MOF membrane

The Zr-MOF membrane aligns with the simulated X-ray diffraction (XRD) pattern, with peaks corresponding to the (111) and (002) reflections at $2\theta = 8.5°$ and 9.8°, respectively (Supplementary Fig. 23)[33]. Different from the most common (111) reflection[10], the (002) reflection becomes the predominant reflection for the Zr-MOF membrane that attains {001} preferential orientation. Nevertheless, no peaks were observed that could be attributed to Zr-MOP (Supplementary Fig. 24)[34], illustrating that the crystal structure of the {001}-oriented Zr-MOF is mostly dominated by the Zr-MOF, while the Zr-MOP does not entirely form. The crystallographic preferential orientation (CPO) indexing method was carried out to estimate the orientation of the {001}-oriented Zr-MOF membrane based on the comparison between the XRD spectrum of the oriented crystalline membrane with that of the simulation of a randomly oriented powder[13,19,35]. The $CPO_{002/111}$ of the Zr-MOF membrane increases progressively with the proportion of Cp_2ZrCl_2 (Fig. 2a). The $CPO_{002/111}$ value reaches 10.08 for the {001}-oriented Zr-MOF membrane when the Cp_2ZrCl_2 content is 5%, which is 23 times higher than the Zr-MOF membrane ($CPO_{002/111} = 0.44$). However, with a further increase in Cp_2ZrCl_2 content, a decrease of $CPO_{002/111}$ is observed due to the incomplete crystal structure of Zr-MOF as a result of the ligand being consumed prematurely (Fig. 2b). More importantly, the recent advances in low-dose electron microscopy enable the high-resolution structural elucidation of beam-sensitive MOF materials[36–41]. By peeling a small piece off the Zr-MOF membrane, the molecular structure can be directly visualized along the [001] direction by low-dose high-resolution transmission electron

https://doi.org/10.1038/s41467-025-64533-5

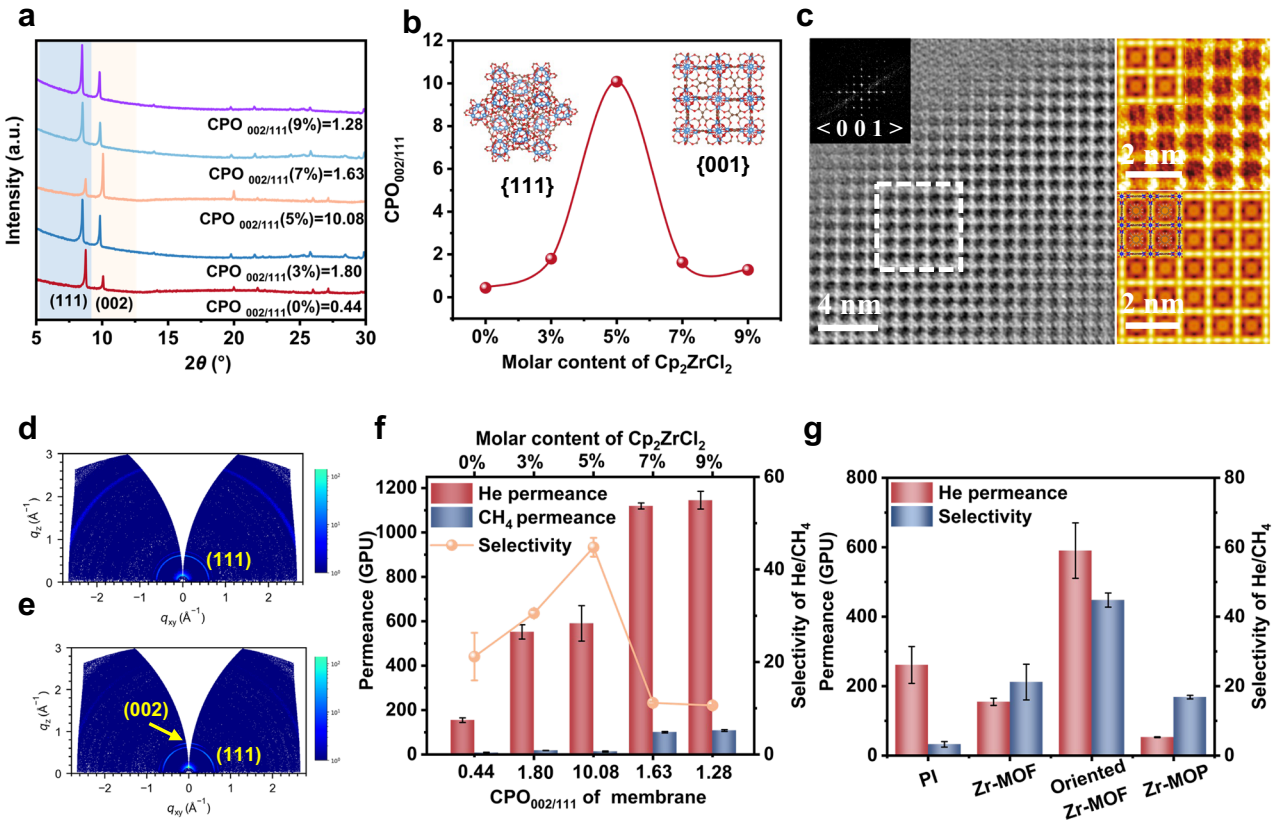

Fig. 2 | Oriented regulation of the Zr-MOF membrane. a XRD spectrum of Zr-MOF membrane with different metallocene-anchor (*x*% represents the Cp_2ZrCl_2 concentration in precursor solution). **b** Effect of different ratios of $ZrCl_4$ and Cp_2ZrCl_2 on the CPO index of Zr-MOF membrane. The Zr, O, and C atoms are represented by blue, red, and brown, respectively. **c** HRTEM image of {001}-oriented Zr-MOF membranes in along the <001> direction. GI-WAXS of (**d**) Zr-MOF and (**e**) {001}-oriented Zr-MOF membranes on silicon wafer. **f** Effect of the CPO index on the He/CH_4 pure-gas separation performance. **g** He/CH_4 pure-gas permeance and ideal selectivity for PI, Zr-MOF, Zr-MOP, and {001}-oriented Zr-MOF membranes.

microscopy (HRTEM). In the false-colored HRTEM image and FFT pattern shown in Fig. 2c, a bright and periodic square pattern is clearly visible, indicating the projected crystal structure of UiO-66 (Zr) with high spatial resolution. This structure consists of $Zr_6O_4(OH)_4$ clusters linked by H_2BDC ligands along the [001] direction. Weak bright contrast can be observed in the middle of these square patterns, referring to the projected H_2BDC linkers. A comparative analysis between the simulated electrostatic potential along the {001} c-axis and the crystalline structure of UiO-66 further confirmed the crystal structure, the lattice orientation, and pore opening of the Zr-MOF membrane as proposed (Fig. 2c). When the Bragg diffraction rings in grazing-incidence wide-angle X-ray scattering (GI-WAXS) appear as complete circles, this indicates a randomly oriented membrane. In contrast, preferred orientation results in arc-like or spot-like diffraction patterns. Compared to the random Zr-MOF membrane (Fig. 2d), the {001}-oriented membrane exhibits distinct arc-shaped diffraction at the (002) facet with an angular spread of approximately 25° (Fig. 2e), further confirming the existence of the {001} oriented structure. The Zr-MOF surface is a special triangular window with pore-aperture sizes ranging from 3.3 to 4.6 Å (Supplementary Fig. 25a)[42]. While the intrinsic dimensions of the triangular windows remain constant across different crystal orientations, their spatial alignment varies significantly. This orientation directly modulates the pathways and the transition energy barriers for gas transport. Compared to the (111) facet (Supplementary Fig. 25e), the triangular window of the (002) facet (Supplementary Fig. 25f) is inclined at a certain angle and possesses a small projected aperture. Calculation of the projected dimensions reveals that the pore-aperture size is 2.7 Å, lying between the kinetic diameters of He (2.6 Å) and CH_4 (3.8 Å). This reduction in the effective triangular aperture size results in the curved diffusion instead of direct penetration for CH_4, thereby enhancing the He/CH_4 selectivity.

Gas separation performance

The influence of $CPO_{002/111}$ on the separation performance of the membrane was investigated as shown in Fig. 2f. Polyimide (PI) was spin-coated onto the surface of Zr-MOF and {001}-oriented Zr-MOF membranes to mitigate the potential of molecular-scale defects (Supplementary Figs. 26 and 27). It should be noted that under the same preparation parameters, the pure PI membrane exhibited a low He/CH_4 selectivity of only 3.2, indicating that PI plays a minimal role in the separation process (Fig. 2g). The electrodeposition time also influences the Zr-MOF membranes separation performance, with an optimal reaction time is 90 min (Supplementary Fig. 28). The concentration of Cp_2ZrCl_2 in precursor solution, which correlates with the metallocene-anchor, obviously influences the membrane separation performance (Fig. 2f). The gas permeance consistently increased with the addition of $CPO_{002/111}$, due to the enhanced metallocene-anchor concentration leading to the formation of more (002) facet, which provide faster gas transmission pathway. When the Cp_2ZrCl_2 content reached 5%, the He/CH_4 selectivity peaked at 44.8, then decreased due to the generation of more defects. The Zr-MOP membrane without the apparent crystal structure and exhibited the lowest permeance (Fig. 2g). Therefore, 5% was selected as the optimal Cp_2ZrCl_2 concentration, with the corresponding {001}-oriented Zr-MOF membrane achieving a He/CH_4 ideal selectivity of 44.8 and the He permeance of 590.4 GPU, which are 2.1 and 3.8 times of the random Zr-MOF

https://doi.org/10.1038/s41467-025-64533-5

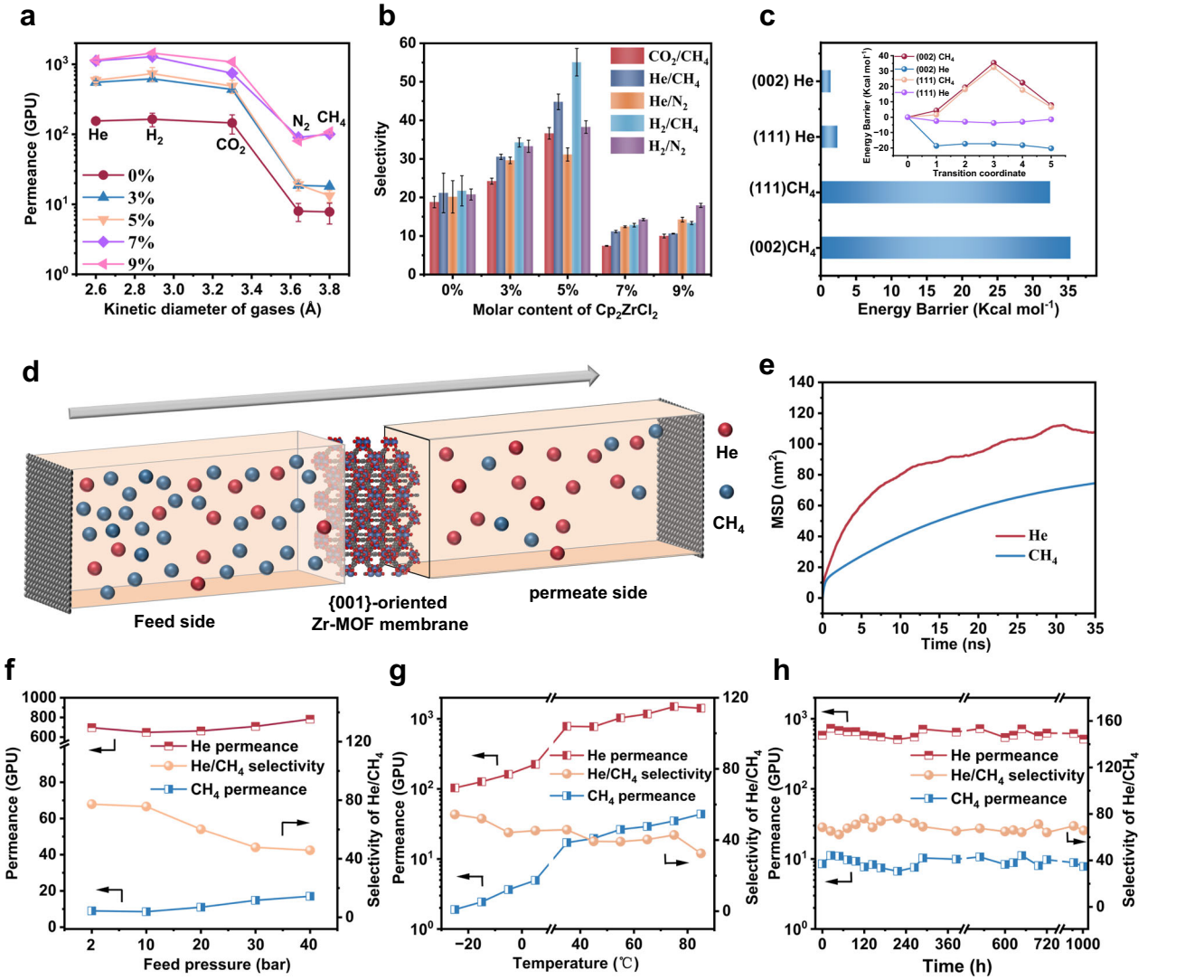

Fig. 3 | Gas permeation performance. a Pure-gas permeance of Zr-MOF membranes as a function of molecular kinetic diameter. (*x*% represents the Cp_2ZrCl_2 concentration in precursor solution). **b** The ideal selectivities of Zr-MOF membranes. **c** The transition energy barrier of He and CH_4 through the oriented Zr-MOF membrane, the inserted graph is energy profiles at different transmission locations. **d** Illustration of the MD simulation. **e** The diffusivities of He and CH_4 through {001}-oriented Zr-MOF membrane. Pressure-dependence (**f**) and temperature-dependence (**g**) of mixed-gas (He/CH_4) for oriented Zr-MOF membrane. **h** Long-term test of the {001}-oriented Zr-MOF membrane.

membrane, respectively. This performance can be ascribed to the addition of metallocene-anchor, which induced the primary crystal facet of the Zr-MOF changing from (111) to the lower atomic packing density orientation of (002).

The permeance of the {001}-oriented Zr-MOF membrane to various gases depends on the kinetic diameter of the gas molecules (Fig. 3a) and is inversely proportional to the kinetic diameter, except for the effect of individual molecular polarization, such as H_2. The gas permeance exhibits a sharp transition between CO_2 and N_2, which suggests that the pore size of the membrane is mainly concentrated between 3.4 and 3.5 Å. The ideal selectivity for He/CH_4, He/N_2, H_2/CH_4, H_2/N_2 and CO_2/CH_4 are 44.8, 31.1, 55.2, 38.4 and 36.7, respectively (Fig. 3b). This strategy also worked for the {001}-oriented Zr-MOF (H_2BDC) membrane with improved selectivity and permeance compared to random Zr-MOF (H_2BDC) membrane (Supplementary Table 2). Furthermore, the performance of the {001}-oriented Zr-MOF (fumarate) membranes with fumarate is superior owing to the larger pore-aperture size of Zr-MOF (H_2BDC) than Zr-MOF (fumarate).

The diffusion energy barrier of gas molecules was calculated based on DFT (Supplementary Figs. 29 and 30). CH_4 requires to overcome a higher transition barrier than He, due to CH_4 with a larger kinetic diameter corresponding to greater steric hindrance (Fig. 3c). Furthermore, due to the inclination of the (002) facet, the energy barrier for CH_4 diffusion through the (002) facet (35.37 Kcal mol^{-1}) is greater than in the (111) facet (32.49 Kcal mol^{-1}), while the energy barrier for He diffusion through the (002) facet (1.38 Kcal mol^{-1}) is lower than in the (111) facet (2.35 Kcal mol^{-1}), confirming the superior He/CH_4 separation performance. The diffusion process of He and CH_4 at the (002) facet (Fig. 3d) and the result shows a simulated snapshot for the 0.3: 99.7 (v/v) He/CH_4 diffuse through the {001}-oriented membrane demonstrated that the diffusion of He is greater than the CH_4 (Fig. 3e and Supplementary Fig. 31). Molecular dynamics (MD) simulations confirmed that the orientation and arrangement of the MOF channels are key to the separation behavior of {001}-oriented MOF membrane.

Usually, the He accounts for a low concentration of 0.01%–0.3% in natural gas, and such a low He content complicates its extraction. Therefore, the impact of operating pressures ranging from 2 to 40 bar

https://doi.org/10.1038/s41467-025-64533-5

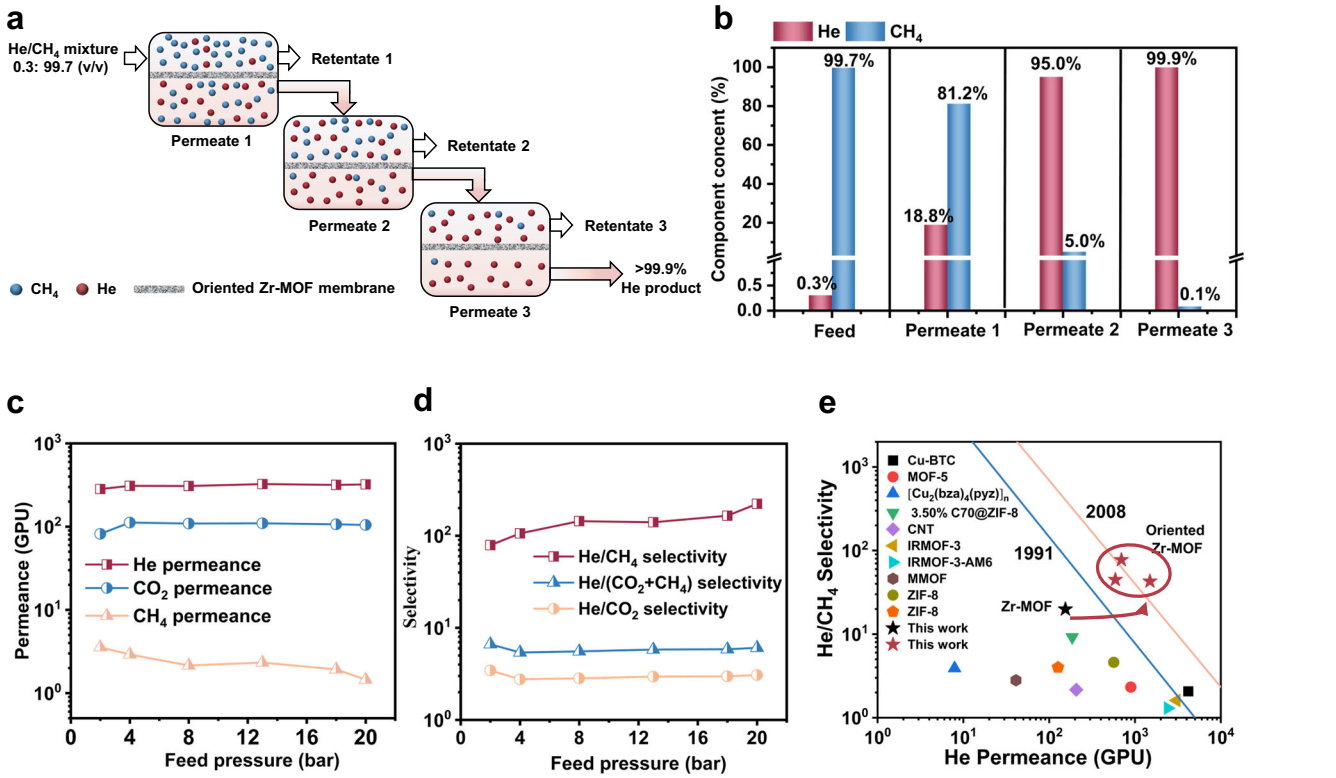

Fig. 4 | Assessment of the separation efficiency of the He recovery. a Schematic representation of the He and CH_4 separation in a low He concentration feed via a three-stage membrane system. **b** The concentration ratio of He and CH_4 in the permeable gas of the three-stage membrane separation system. Mixed-gas ($He/CO_2/CH_4$) (0.3/49.7/50, v/v/v) **c** permeance and **d** selectivity performance of the {001}-oriented Zr-MOF membrane with different pressure. **e** Comparison of the He/CH_4 separation performance of membranes in literature. (The Robeson upper bound is assumed to be 1 μm membrane thickness; for more information, see Supplementary Table 3).

on separation performance was tested using a 0.3: 99.7 (v/v) He/CH_4 mixture, which more closely approximates the composition of actual natural gas. The separation performance for the 0.3: 99.7 (v/v) He/CH_4 mixture was found to be superior to that of the pure gas, which can be explained by the pressure effect[17,43]. With the pressure increased from 2 to 40 bar, the permeance of He remains unchanged while gradually increasing for the CH_4, leading to a decrease in He/CH_4 selectivity from 77.3 to 45.8 (Fig. 3f and Supplementary Fig. 32). Meanwhile, the effect of temperature on the membrane separation performance was explored under a high pressure of 40 bar to further evaluate the feasibility of the membrane in practical applications. As the temperature increased from −25 °C to 85 °C, the permeance of He and CH_4 increased, while the selectivity decreased due to the higher apparent activation energy of CH_4 (22.15 KJ mol^{-1}) than that of He (19.77 KJ mol^{-1}) (Fig. 3g and Supplementary Fig. 33). The separation performance is higher than the Robeson upper bound at high temperature (Supplementary Fig. 34). Furthermore, the long-term stability of the {001}-oriented Zr-MOF membrane was conducted for 1000 h, proving the long-term stability of the membrane (Fig. 3h). Meanwhile, the {001}-oriented Zr-MOF membrane also remains stable under humid condition (Supplementary Fig. 35).

We have designed a three-stage membrane separation system to concentrate the He from low concentration feedstock (Fig. 4a). A 0.3:99.7 (v/v) He/CH_4 mixture is introduced into the primary membrane separation system, the He concentration is concentrated to 18.8%. Following passing through the three-stage membrane separation system, the He concentration reaches >99.9% (Fig. 4b), meeting the He purity requirement for industrial uses. Furthermore, a mixture-gas ($He/CO_2/CH_4$) (0.3/49.7/50, v/v/v) at 2 bar was tested; the permeance is lower than that of the pure-gas permeance due to the competitive adsorption[44]. The membranes offered He and CO_2 permeance of 282.8 and 81.8 GPU, respectively, and He/CH_4 and CO_2/CH_4 selectivities of 79.5 and 23.0, respectively (Fig. 4c, d). Taking CO_2 and CH_4 as an integrated impurity, the $He/(CO_2 + CH_4)$ selectivity is 6.6. Meanwhile, the selectivity remains stable with the increase of feed pressure, indicating the potential for the membrane to be applied in a practical He extract process. Overall, this {001}-oriented Zr-MOF membrane demonstrates advantages in comprehensive performance over previously reported membranes (Fig. 4e, Supplementary Fig. 36 and Supplementary Table 3).

In conclusion, efficient separation of He and CH_4 was achieved by regulating the growth of MOF along the c-axis with the assistance of the metallocene-anchor and electric field. The MOP fragment was employed as the metallocene-anchor, with a lower coordination potential energy barrier, generating preferentially in the precursor solution and then inducing the vertical growth of {001}-oriented Zr-MOF membrane. The oriented MOF provides rapid transport channels for He, and the unique (002) facet enhances the sieving effect of He/CH_4, resulting in a high He/CH_4 separation performance. Additionally, He enrichment (>99.9%) can be obtained through a three-stage membrane separation process using the {001}-oriented Zr-MOF membrane. This work presents a strategy for fabricating highly oriented MOF membranes and possesses potential in He recovery from natural gas.

Methods

Materials

AAO with a pore size of 20 nm (AAO, diameter of 13 mm) was obtained from GE Whatman. Fumarate (≥99.0%), terephthalic acid (≥99.0%), bis(cyclopentadienyl) zirconium (IV) dichloride (Cp_2ZrCl_2, ≥98%),

2,4,6-trimethyl-1,3-phenylenediamine (DAM, 99.0%), and 4,4′-(Hexafluoroisopropylidene) diphthalic anhydride (6FDA, 99.6%) were purchased from Sigma-Aldrich. Dimethyl sulfoxide (DMSO, 99.0%), Zirconium chloride ($ZrCl_4$, ≥98%), acetate (≥99.5%), pyridine (99.5%), 1-methyl-2-pyrrolidinone (NMP, 99.5%), and *N*, *N*-Dimethylformamide (DMF, 99.8%) were provided by Aladdin. Lithium nitrate ($LiNO_3$, ≥99.9% metals basis) was obtained from Macklin. Acetic anhydride was obtained from Sinopharm Chemical Reagent. All used chemical regents were used without further purification.

Preparation of precursor solutions and membranes

Precursor solutions preparation for Zr-MOF membrane. Fumarate (50 mM), $ZrCl_4$ (25 mM), and 3–4 drops of deionized water were added to 20 mL DMSO. Mon-acid (such as acetic acid) was added as a regulator, and $LiNO_3$ (200 mM) was added to promote the electrodeposition reaction. The solution was under ultrasonication for 20 min. The Zr-MOP membrane precursor solution was prepared by replacing $ZrCl_4$ with Cp_2ZrCl_2, and the solution was DMA.

Precursor solutions preparation for {001}-oriented Zr-MOF membrane. Fumarate (50 mM), $ZrCl_4$ (23.75 mM), Cp_2ZrCl_2 (1.25 mM), and 3–4 drops of deionized water were added to 20 mL DMSO, and mon-acid (such as acetic acid) was added as a regulator. $LiNO_3$ (200 mM) was added to promote the electrodeposition reaction, and the solution under ultrasonication for 20 min to prepare the {001}-oriented Zr-MOF ($ZrCl_4$: Cp_2ZrCl_2, 95:5) precursor solution. Other ratios were added to maintain the total concentration of $ZrCl_4$ and Cp_2ZrCl_2 at 25 mM. Meanwhile, fumarate can be replaced with terephthalic acid.

Electrochemical synthesis of membranes. The AAO substrate was coated with platinum (40 mA, 100 s) via sputtering deposition. The Pt-coated AAO membrane was soaked in the precursor solution, serving as the working electrode at a current density of −10 mA cm^{-2}, while the Pt electrode acted as the counter electrode, with the process conducted at 120 °C for 90 min. After removal from the electrode, the membrane was gradually cooled, washed three times with methanol, and dried under ambient conditions to yield Zr-MOF and oriented Zr-MOF membranes. To prepare membranes for GI-WAXS characterization, AAO was replaced with silicon wafers. Polyimide (PI) was spin-coated onto the surface of the Zr-MOF and {001}-oriented Zr-MOF membranes to minimize potential molecular-scale defects. A 10 wt% solution of PI was initially spin-coated onto the membranes at 2000 rpm for 60 s, followed by drying at 80 °C in an oven. Pure PI membranes were prepared under the same conditions. The measurement of gas permeation of the membranes was provided in Supplementary Fig. 37.

Characterization

The morphology of several series of membranes was examined using SEM (Hitachi SU-8020), and the membrane roughness was further analyzed with AFM (Icon ScanAsyst, Bruker). The image of {001}-oriented Zr-MOF membranes along the <001> direction was obtained by HRTEM (Spectra 300, Thermo Scientific). The chemical composition was characterized by ATR-FTIR (NICOLET 380, Thermo Scientific). XRD patterns were obtained using a Rigaku SMART LAB diffractometer with CuKα radiation (wavelength $\lambda = 1.5418$). GI-WAXS (Xeuss 2.0) was employed to investigate the crystal structure of the membranes on a silicon wafer. XPS (ESCALAB250Xi, Thermo Scientific) was used to determine the elemental composition on the membrane surface. The specific surface area of particles collected from the membrane surface was measured via N_2 adsorption isotherms (BET, AutoChem II2920, Micromeritics). EXAFS was utilized to analyze the coordination environment of Zr metal. Data analysis and EXAFS fitting were performed using the Athena and Artemis programs within the Demeter data analysis package[45,46].

DFT simulation. DFT simulations were performed using the Vienna ab initio simulation package, which utilizes plane-wave basis sets combined with the projector augmented-wave method[47,48]. The exchange-correlation potential was handled using the generalized gradient approximation with the Perdew–Burke–Ernzerhof parametrization[49]. Furthermore, Grimme's DFT-D3 model was applied by der Waals correction[50]. The energy cut-off was set to 520 eV. A 1 × 1 × 1 Γ-centered Monkhorst-Pack mesh was applied to sample the Brillouin-zone integration[51]. The structures were fully relaxed until the maximum force on each atom was less than 0.02 eV $Å^{-1}$. Meanwhile, the energy convergence criterion is 10^{-5} eV. During the optimization, the structure was fully relaxed to the minimum energy principle.

MD simulation. MD simulation of the directed diffusion of a He/CH_4 mixture in Zr-MOF was carried out using the Gromacs program suite, employing a hybridized force field composed of TraPPE-Small[52] and UFF4MOFII force fields[53–55]. He and CH_4 were modeled using the TraPPE-Small parameters. The Zr-MOF slab models of the (002) facet were parameterized with the UFF4MOFII force field. Topology files of these molecules and crystals were generated directly via the AuToFF web server.

The initial simulation boxes for the (002) facet consisted of two vacuum layers, 80 nm thick, with a graphene layer inserted between them to ensure periodic boundary conditions in all directions. There were 5000 molecules of 0.3:99.7 (v/v) He/ CH_4 on one side of the vacuum layers at the initial state. The system was first energy-minimized before undergoing an MD simulation for a total duration of 35 ns in the NVT ensemble. Trajectory data was recorded every 50 ps. The temperature was maintained at 308.15 K using the velocity-rescale thermostat with a 1 ps relaxation constant. Electrostatic interactions and van der Waals forces were treated using the Particle Mesh Ewald method, with a truncation distance of 15 Å.

Data availability

The data that support the findings of this study are available in the article and the Supplementary Information, or are available from the corresponding author upon request. Source data are provided with this paper.

References

1. Nuttall, W. J., Clarke, R. H. & Glowacki, B. A. Stop squandering helium. *Nature* **485**, 573–575 (2012).
2. Zhang, C. & Koros, W. J. Ultraselective carbon molecular sieve membranes with tailored synergistic sorption selective properties. *Adv. Mater.* **29**, 1701631 (2017).
3. Welch, R. V. Helium—What about it?. *J. Can. Petrol. Technol.* **13**, 3–18 (1985).
4. Lin, J. Y. S. Molecular sieves for gas separation. *Science* **353**, 121–122 (2016).
5. Zhou, S. et al. Asymmetric pore windows in MOF membranes for natural gas valorization. *Nature* **606**, 706–712 (2022).
6. Zhou, S. et al. Paralyzed membrane: current-driven synthesis of a metal-organic framework with sharpened propene/propane separation. *Sci. Adv.* **4**, 1393 (2018).
7. Liu, G. et al. Eliminating lattice defects in metal-organic framework molecular-sieving membranes. *Nat. Mater.* **22**, 769–776 (2023).
8. Sun, Y. et al. In-plane epitaxial growth of highly c-oriented NH_2-MIL-125(Ti) membranes with superior H_2/CO_2 selectivity. *Angew. Chem. Int. Ed.* **57**, 16088–16093 (2018).
9. Liu, Y., Zeng, G., Pan, Y. & Lai, Z. Synthesis of highly c-oriented ZIF-69 membranes by secondary growth and their gas permeation properties. *J. Membr. Sci.* **379**, 46–51 (2011).
10. Sun, Y. et al. Fabrication of highly oriented ultrathin zirconium metal-organic framework membrane from nanosheets towards

unprecedented gas separation. *Angew. Chem. Int. Ed.* **62**, e202216697 (2023).
11. Wang, S. et al. Oriented titanium-MOF membrane for hydrogen purification. *Angew. Chem. Int. Ed.* **64**, e202413701 (2025).
12. Bux, H. et al. Oriented zeolitic imidazolate framework-8 membrane with sharp H_2/C_3H_8 molecular sieve separation. *Chem. Mater.* **23**, 2262–2269 (2011).
13. Jeong, H.-K., Krohn, J., Sujaoti, K. & Tsapatsis, M. Oriented molecular sieve membranes by heteroepitaxial growth. *J. Am. Chem. Soc.* **124**, 12966–12968 (2002).
14. Xu, L.-H. et al. Highly flexible and superhydrophobic MOF nanosheet membrane for ultrafast alcohol-water separation. *Science* **378**, 308–313 (2022).
15. Shekhah, O. et al. Step-by-step route for the synthesis of metal-organic frameworks. *J. Am. Chem. Soc.* **129**, 15118–15119 (2007).
16. Makiura, R. et al. Surface nano-architecture of a metal-organic framework. *Nat. Mater.* **9**, 565–571 (2010).
17. Wei, R. et al. Carbon nanotube supported oriented metal organic framework membrane for effective ethylene/ethane separation. *Sci. Adv.* **8**, eabm6741 (2022).
18. Wu, Q. et al. Highly (222)-oriented flexible hollow fiber-supported metal-organic framework membranes for ultra-permeable and selective H_2/CO_2 separation. *Chem. Eng. J.* **461**, 141976 (2023).
19. Xu, R., Kang, Y., Zhang, W., Zhang, X. & Pan, B. Oriented uio-67 metal-organic framework membrane with fast and selective lithium-ion transport. *Angew. Chem. Int. Ed.* **61**, e202115443 (2022).
20. Yan, J. et al. Facile synthesis of oriented Zr-MOF membrane under complete room-temperature condition with superb selectivity for carbon capture. *Ind. Eng. Chem. Res.* **62**, 5973–5983 (2023).
21. Panda, S., Kundu, S., Malik, P. & Haldar, R. Leveraging metal node-linker self-assembly to access functional anisotropy of zirconium-based MOF-on-MOF epitaxial heterostructure thin films. *Chem. Sci.* **15**, 2586–2592 (2024).
22. Yan, J. et al. Room temperature fabrication of oriented Zr-MOF membrane with superior gas selectivity with zirconium-oxo cluster source. *J. Membr. Sci.* **661**, 120959 (2022).
23. Yan, J. et al. Cooperative defect tailoring: a promising protocol for exceeding performance limits of state-of-the-art MOF membranes. *J. Membr. Sci.* **635**, 119515 (2021).
24. Jiao, J. et al. Design and assembly of chiral coordination cages for asymmetric sequential reactions. *J. Am. Chem. Soc.* **140**, 2251–2259 (2018).
25. Mugridge, J. S., Zahl, A., van Eldik, R., Bergman, R. G. & Raymond, K. N. Solvent and pressure effects on the motions of encapsulated guests: tuning the flexibility of a supramolecular host. *J. Am. Chem. Soc.* **135**, 4299–4306 (2013).
26. Zhou, S. et al. Electrochemical synthesis of continuous metal-organic framework membranes for separation of hydrocarbons. *Nat. Energy* **6**, 882–891 (2021).
27. Xie, S. et al. Cathodic deposition-assisted synthesis of thin glass MOF films for high-performance gas separations. *Angew. Chem. Int. Ed.* **63**, e202401817 (2024).
28. Yu, Z. et al. Preparation, cross-linking and ceramization of AHPCS/Cp_2ZrCl_2 hybrid precursors for SiC/ZrC/C composites. *J. Eur. Ceram. Soc.* **32**, 1291–1298 (2012).
29. Qiao, Z. et al. Ultrathin low-crystallinity MOF membranes fabricated by interface layer polarization induction. *Adv. Mater.* **32**, 2002165 (2020).
30. Li, P., Chen, I. W. & Penner-Hahn, J. E. Effect of dopants on zirconia stabilization—an X-ray absorption study: I, Trivalent Dopants. *J. Am. Ceram. Soc.* **77**, 118–128 (1994).
31. Su, Z., Miao, Y.-R., Zhang, G., Miller, J. T. & Suslick, K. S. Bond breakage under pressure in a metal organic framework. *Chem. Sci.* **8**, 8004–8011 (2017).
32. Guo, B. et al. Dehydrated UiO-66$(SH)_2$: the Zr–O cluster and its photocatalytic role mimicking the biological nitrogen fixation. *Angew. Chem. Int. Ed.* **61**, e202117244 (2022).
33. Furukawa, H. et al. Water adsorption in porous metal-organic frameworks and related materials. *J. Am. Chem. Soc.* **136**, 4369–4381 (2014).
34. Pastore, V. J. et al. Clickable norbornene-based zirconium carboxylate polyhedra. *Chem. Mater.* **35**, 1651–1658 (2023).
35. Cheng, L. et al. Fabrication and orientation of Ni-LAB membranes by linker salt approach. *Microporous Mesoporous Mater.* **287**, 135–143 (2019).
36. Zhu, Y. et al. Unravelling surface and interfacial structures of a metal–organic framework by transmission electron microscopy. *Nat. Mater.* **16**, 532–536 (2017).
37. Chen, Q. et al. Imaging beam-sensitive materials by electron microscopy. *Adv. Mater.* **32**, 1907619 (2020).
38. Zhang, W. et al. Metal-halide porous framework superlattices. *Nature* **638**, 418–424 (2025).
39. Zhan, G. et al. Moiré two-dimensional covalent organic framework superlattices. *Nat. Chem.* **17**, 518–524 (2025).
40. Xu, X. et al. Unravelling nonclassical beam damage mechanisms in metal-organic frameworks by low-dose electron microscopy. *Nat. Commun.* **16**, 261 (2025).
41. Liu, Y. et al. Revolutionizing the structural design and determination of covalent–organic frameworks: principles, methods, and techniques. *Chem. Soc. Rev.* **53**, 502–544 (2024).
42. Liu, Y. et al. Conformation-controlled molecular sieving effects for membrane-based propylene/propane separation. *Adv. Mater.* **31**, 1807513 (2019).
43. Liu, D., Ma, X., Xi, H. & Lin, Y. S. Gas transport properties and propylene/propane separation characteristics of ZIF-8 membranes. *J. Membr. Sci.* **451**, 85–93 (2014).
44. Wang, C. et al. Dual thermally crosslinked hollow fiber membranes for plasticization-resistant helium recovery from natural gas. *Sep. Purif. Technol.* **354**, 129019 (2025).
45. Zabinsky, S. I., Rehr, J. J., Ankudinov, A., Albers, R. C. & Eller, M. J. Multiple-scattering calculations of x-ray-absorption spectra. *Phys. Rev. B* **52**, 2995–3009 (1995).
46. Ravel, B. & Newville, M. ATHENA, ARTEMIS, HEPHAESTUS: data analysis for X-ray absorption spectroscopy using IFEFFIT. *J. Synchrotron Radiat.* **12**, 537–541 (2005).
47. Blöchl, P. E. Projector augmented-wave method. *Phys. Rev. B* **50**, 17953–17979 (1994).
48. Kresse, G. & Furthmüller, J. Efficient iterative schemes for ab initio total-energy calculations using a plane-wave basis set. *Phys. Rev. B* **54**, 11169–11186 (1996).
49. Perdew, J. P., Burke, K. & Ernzerhof, M. Generalized gradient approximation made simple. *Phys. Rev. Lett.* **77**, 3865–3868 (1996).
50. Grimme, S., Antony, J., Ehrlich, S. & Krieg, H. A consistent and accurate ab initio parametrization of density functional dispersion correction (DFT-D) for the 94 elements H-Pu. *J. Chem. Phys.* **132**, 154104 (2010).
51. Monkhorst, H. J. & Pack, J. D. Special points for Brillouin-zone integrations. *Phys. Rev. B* **13**, 5188–5192 (1976).
52. Zhang, L. & Siepmann, J. I. Direct calculation of Henry's law constants from Gibbs ensemble Monte Carlo simulations: nitrogen, oxygen, carbon dioxide and methane in ethanol. *Theor. Chem. Acc.* **115**, 391–397 (2006).
53. Coupry, D. E., Addicoat, M. A. & Heine, T. Extension of the universal force field for metal–organic frameworks. *J. Chem. Theory Comput.* **12**, 5215–5225 (2016).
54. Addicoat, M. A., Vankova, N., Akter, I. F. & Heine, T. Extension of the universal force field to metal-organic frameworks. *J. Chem. Theory Comput.* **10**, 880–891 (2014).

55. Rappé, A. K., Casewit, C., Colwell, K. S., Goddard, W. A. & Skiff, W. M. UFF, a full periodic table force field for molecular mechanics and molecular dynamics simulations. *J. Am. Chem. Soc.* **114**, 10024–10035 (1992).

Acknowledgements

This work is financially supported by the National Natural Science Foundation of China (22322801 by H.F.), the Project of Stable Support for Youth Team in Basic Research Field of CAS (YSBR-017 by L.S.), CAS Project for Young Scientists in Basic Research (YSBR-038 by L.S.), and Fundamental Research Funds for the Central Universities (buctrc202135 by H.F.).

Author contributions

S.Z., H.F., and L.S. conceived the idea and revised the manuscript. J.B. designed and carried out most of the experiments and drafted the manuscript. L.X. and H.L. captured SEM and AFM images. Y.Z. captured and analyzed TEM images. C.W. performed gas permeation experiments. X.Z., L.G., and S.L. discussed and revised the manuscript. All authors contributed to the draft of the paper.

Competing interests

The authors declare no competing interests.

Additional information

Supplementary information The online version contains supplementary material available at https://doi.org/10.1038/s41467-025-64533-5.

Correspondence and requests for materials should be addressed to Linglong Shan, Hongwei Fan or Suojiang Zhang.

Peer review information *Nature Communications* thanks Xiuling Chen, Zhongde Dai, and the other, anonymous, reviewer(s) for their contribution to the peer review of this work. A peer review file is available.

Reprints and permissions information is available at http://www.nature.com/reprints

Publisher's note Springer Nature remains neutral with regard to jurisdictional claims in published maps and institutional affiliations.

Open Access This article is licensed under a Creative Commons Attribution-NonCommercial-NoDerivatives 4.0 International License, which permits any non-commercial use, sharing, distribution and reproduction in any medium or format, as long as you give appropriate credit to the original author(s) and the source, provide a link to the Creative Commons licence, and indicate if you modified the licensed material. You do not have permission under this licence to share adapted material derived from this article or parts of it. The images or other third party material in this article are included in the article's Creative Commons licence, unless indicated otherwise in a credit line to the material. If material is not included in the article's Creative Commons licence and your intended use is not permitted by statutory regulation or exceeds the permitted use, you will need to obtain permission directly from the copyright holder. To view a copy of this licence, visit http://creativecommons.org/licenses/by-nc-nd/4.0/.

© The Author(s) 2025